Energy Technology

Energy Technology
Generation, Conversion, Storage, Distribution

RESEARCH ARTICLE OPEN ACCESS

Influence of Bimetallic Catalysts on Hydrogen Yield and H_2:CO Syngas Ratio From the Pyrolysis-Catalytic Steam Reforming of Polypropylene

Fayez Alshehri[1,2] | Paul T. Williams[1]

[1]School of Chemical and Process Engineering, University of Leeds, Leeds, UK | [2]Institute of Earth and Space Sciences, King Abdulaziz City for Science and Technology, Riyadh, Saudi Arabia (On secondment to the University of Leeds)

Correspondence: Paul T. Williams (p.t.williams@leeds.ac.uk)

Received: 10 February 2026 | **Revised:** 20 May 2026 | **Accepted:** 23 June 2026

Keywords: catalysis | hydrogen | syngas | waste plastic

ABSTRACT

Pyrolysis-catalytic steam reforming of polypropylene has been investigated using bimetallic-alumina catalysts to determine the influence on hydrogen yield, H_2:CO syngas ratio, and catalyst coke formation. The presence of different metals coupled with nickel significantly influences the reforming process, for example, producing high hydrogen yield (>100 mmol $g^{-1}_{plastic}$), defined H_2:CO ratio (between 1.96 and 3.41), or heavy catalyst coking. For example, the Ni-Cu/Al_2O_3 catalyst produced a H_2 yield of 99.13 mmol $g^{-1}_{plastic}$, H_2:CO ratio of 3.41, but with high catalyst coke deposition of 15.76 wt%. Whereas, the Ni-Mg/Al_2O_3 catalyst gave a H_2 yield of 92.19 mmol $g^{-1}_{plastic}$, H_2:CO ratio of 2.56, and moderate coke deposition of 6.60 wt%. The Ni-Mn/Al_2O_3 and Ni-Mo/Al_2O_3 catalysts gave hydrogen yields of 87.55 and 82.26 mmol $g^{-1}_{plastic}$, respectively. Bimetallic catalysts containing no Ni, such as Fe-Co/Al_2O_3, and Co-Cu/Al_2O_3, showed reduced H_2 yield and H_2:CO syngas ratio. The results highlight the critical role of active metal choice and loading in maximising hydrogen production and minimising catalyst coking. Nickel remains the most effective reforming metal, while carefully designed bimetallic catalysts, particularly those containing Co, Mo, or Mg, offer targeted gains in hydrogen selectivity, targeted H_2:CO ratio, or catalyst coke resistance.

1 | Introduction

The rapid growth in worldwide plastic production, currently totalling more than 450 million tonnes per year, has resulted in a significant waste management problem. The OECD Global Plastics Outlook indicates that only 9% of plastic waste is recycled; the majority is incinerated (19%), landfilled (50%), or mismanaged (22%), resulting in considerable environmental leakage that causes pollution and damages ecosystems [1]. Hydrogen is emerging as a fundamental element of sustainable energy initiatives, including the decarbonisation of transportation, electricity generation, and industry. Nevertheless, over 80% of worldwide H_2 production is derived via steam methane reforming (SMR) of fossil fuel natural gas, which generates around 9–12 tonnes of CO_2 per tonne of H_2 [2, 3]. Other renewable and non-renewable routes for hydrogen generation, including electrolysis, biochemical, and photo-electric methods, are assessed as more sustainable [4], but are constrained by financial and infrastructural challenges [5]. Pyrolysis combined with catalytic steam reforming of plastic waste presents a novel alternative option for hydrogen production [6–8]. This two-stage method involves the pyrolysis of plastic waste at ~500°C to generate volatile hydrocarbons from the thermal degradation of the plastic polymer, followed by steam reforming of the evolved hydrocarbons at ~800°C over a suitable catalyst [6–8]. In principle, the process is similar to the catalytic steam reforming of natural gas (Equation (1)); however, the hydrocarbons produced from the pyrolysis of waste plastic are much more complex than

natural gas. For example, pyrolysis of polypropylene and polyethylene generate linear alkanes, alkenes, and alkadienes hydrocarbons ranging from carbon number C_1 to over C_{50}, whereas pyrolysis of waste polystyrene produces a highly aromatic hydrocarbon product slate [9]. The catalytic steam reforming of these higher hydrocarbons is a more complex process (particularly for aromatic hydrocarbons) than natural gas steam reforming, leading to un-reformed and thermal/catalytically cracked hydrocarbons and generating higher catalyst coke formation [6, 8, 10].

$$CH_4 + H_2O \rightarrow CO + 3H_2 \quad (1)$$

The process of hydrogen production from the two-stage pyrolysis-catalytic steam reforming of waste plastics is influenced by several process parameters. For example, different plastic types will produce different yields of hydrogen under the same reaction conditions because the variable hydrocarbon composition of the volatiles from the pyrolysis of the different plastics will greatly influence the catalytic steam reforming process [11]. The process conditions, including catalyst temperature [12], plastic: catalyst ratio [13], rate of steam input [14], etc., all influence the yield of hydrogen.

Noble metals such as Rh, Ru, and Pd have been investigated, but the most common metals used are transition metals due to their lower costs, ready availability, and activity towards reforming for hydrogen production [15]. A variety of support materials have also been used, such as MCM-41, zeolite, and silica, but alumina remains the most widely used. Consequently, nickel-alumina (Ni/Al_2O_3) is the most researched catalyst for the production of hydrogen from waste plastics. Indeed, the Ni/Al_2O_3 catalyst is widely used for the commercial production of hydrogen from the catalytic steam reforming of natural gas due to its high catalytic activity for methane reforming and cost-effectiveness compared to noble metals [15]. Investigations into new catalysts for the commercial process have included alternative monometallic, such as Co/Al_2O_3 and Cu/Al_2O_3, and bimetallic catalysts such as $Ni\text{-}Co/Al_2O_3$ and $Ni\text{-}Cu/Al_2O_3$ [15]. Another issue around the use of Ni/Al_2O_3 catalyst is then tendency for carbon deposition on the catalyst, resulting in catalyst deactivation [16]. An issue that would be particularly problematic for the reforming of the complex mixture of high molecular weight hydrocarbons produced from the pyrolysis of waste plastics [17].

Therefore, there is a need to research alternative transition metals and bimetallic catalytic systems to improve the catalysts in terms of hydrogen production performance and catalyst durability, particularly related to the plastics pyrolysis-catalytic steam reforming process. However, while several monometallic transition metals and bimetallic catalysts supported on Al_2O_3 have been studied, such research has largely remained empirical. Previous studies typically test multiple variables simultaneously, such as support type, metal loading, and varying reaction conditions, complicating the isolation of unique metal effects. Furthermore, the existing literature often lacks the deep mechanistic insights required to explain structural stability and coke suppression behaviour at the molecular level.

To address this gap and provide new scientific understanding, this study systematically investigates the production of hydrogen and syngas from the pyrolysis-catalytic steam reforming of waste plastic using carefully controlled bimetallic catalyst formulations. Nickel with added metal promoters (Fe, Co, Cu, Mg, Mn, Mo) supported on Al_2O_3 were evaluated alongside Ni-free bimetallic combinations (Mn-Mo, Fe-Co, Co-Cu). Crucially, by keeping all other process parameters strictly constant, this experimental design isolates metal composition as the principal variable. The novel contribution of this work lies in moving beyond descriptive performance metrics by explicitly linking specific bimetallic synergy mechanisms, such as Mars-van-Krevelen (MvK) redox cycles, reverse Boudouard reactions, and dynamic phase segregations directly to quantitative coke suppression behaviour and syngas purity. Ultimately, this study establishes a fundamental baseline for the future design of optimised, coke-resistant multi-metallic catalysts for sustainable hydrogen production.

2 | Materials and Methods

2.1 | Waste Plastic Feedstock

Polypropylene was in the form of recycled waste plastic pellets of 1–2 mm size, which were used as feedstock, supplied by Beijing Ou Yuan Sheng Plastic Production Co. An ultimate analysis was carried out using a Thermo Flash EA2000 to quantify the elemental composition of the plastic. The analysis revealed 82.03 wt% carbon, 16.55 wt% hydrogen, 0.36 wt% nitrogen, and 1.07 wt% oxygen, with no sulphur identified. The presence of other elements apart from carbon and hydrogen was expected due to the possible presence of impurities, additives, or minor contents of other plastics during the recycling process. Proximate analysis, using a Shimadzu TGA-50 thermogravimetric analyser, was also conducted for proximate analysis and showed the plastic sample contained 95.30 wt% volatiles, 6.04 wt% ash, and 0.03 wt% fixed carbon.

2.2 | Catalyst Preparation

The range of different Ni-based bimetallic catalysts and bimetallic catalysts without Ni (Mn-Mo, Fe-Co, Co-Cu) were prepared using the wet impregnation technique, supported on Al_2O_3. The bimetallic-based catalysts were synthesised from their associated precursor salts in a 1:1 basis of each active metal at 5 wt% loadings, producing bimetallic catalysts at 10 wt% of metal. Table 1 presents all the precursor salts, supports, and chemical suppliers.

The catalyst preparation procedure involve; calculation of the precursor salt amount mixed with 20 ml of deionised water; solution is heated on a hot plate stirrer to 40°C and maintained for 20 min: Al_2O_3 sized to 50–212 μm, added to the solution and mixed for a further 15 min; temperature is raised gradually to 100°C so that all water moisture is evaporated and the mixture becomes semi-solid. The prepared sample is then placed in an oven at 105°C for 24 h, then calcined at 750°C for 3 h. Finally, the catalyst is reduced in a furnace supplied with 5 vol% H_2 (95 vol% N_2) at a temperature of 800°C for 3 h.

TABLE 1 | Details of precursor salts and Al_2O_3 that were utilised for catalyst preparations.

Active phase	Precursor salt	Chemical formula	Supplier
Ni	Nickel(II) nitrate hexahydrate	$Ni(NO_3)_2{\cdot}6H_2O$	Alfa Aesar
Fe	Iron(III) nitrate nonahydrate	$Fe(NO_3)_3{\cdot}9H_2O$	VWR International
Co	Cobalt(II) nitrate hexahydrate	$Co(NO_3)_2{\cdot}6H_2O$	Fisher Scientific Ltd
Cu	Copper(II) Nitrate Hemi(Pentahydrate)	$Cu(NO_3)_2{\cdot}2.5H_2O$	Alfa Aesar
Mg	Magnesium nitrate hexahydrate	$Mg(NO_3)_2{\cdot}6H_2O$	Merck Life Science
Mn	Manganese(II) perchlorate hexahydrate	$Mn(ClO_4)_2{\cdot}6H_2O$	Alfa Aesar
Mo	Ammonium molybdate (para) tetrahydrate	$(NH_4)_6\ Mo_7O_{24}{\cdot}4H_2O$	Merck Life Science
Support	Aluminium oxide	Al_2O_3	Alfa Aesar

2.3 | Pyrolysis-Catalytic Steam Reforming Experimental System

The pyrolysis-catalytic steam reforming of waste polypropylene in relation to the different bimetallic catalysts was investigated using an experimental two-stage fixed-bed batch reactor system, shown as a schematic diagram in Figure 1. The reactor material was stainless steel and consisted of a pyrolysis zone and a catalytic reforming zone, separately heated by external electrical furnaces. Temperature was monitored and controlled throughout the experiments. The polypropylene waste plastic sample was placed in a stainless-steel crucible located centrally in the pyrolysis reactor, and the catalyst was placed in the reforming reactor consisting of a fixed bed of catalyst. Steam was supplied from water and syringe pump set to 4 mL/h. Nitrogen was purged through the reactor system continuously. The product gas condensation system consisted of three water and dry-ice condensers followed by non-condensable gas collection in a 25 L Tedlar gas collection sample bag. In all experiments, 1 g of polypropylene was used, the catalyst mass was 1 g held at a temperature fixed at 800°C, and the pyrolysis temperature programme was 20°C–500°C at a heating rate of 20°C min^{-1}, followed by a hold for 20 min. and the steam-to-plastic flow rate was 4 g/h.

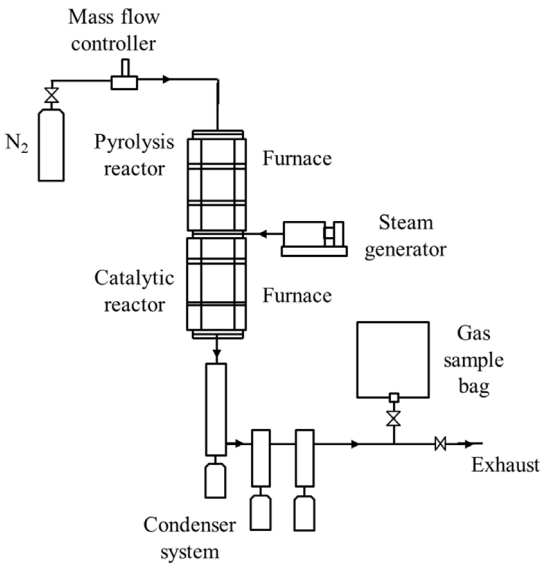

FIGURE 1 | Schematic diagram of the two-stage pyrolysis-catalytic steam reforming experimental fixed-bed reactor system.

2.4 | Product Analysis and Catalysts Characterisation

Product gases were analysed using a Varian CP-3330 gas chromatograph (GC) fitted with a 2-meter-long and 2-millimetre-diameter HayeSep packed column to determine the relative amounts of permanent gases: H_2, N_2, O_2, and CO. The GC column had a mesh size of 60–80 mm and was operated with an argon carrier gas. The GC instrument was equipped with a thermal conductivity detector (TCD). Due to the comparable retention durations of CO and CO_2, the analysis for CO_2 had to be conducted using a different Varian CP-3330 instrument, working under the same conditions but with a smaller mesh size (80–100 mm) column. An analysis of hydrocarbon gases was conducted using a Varian CP-3380 GC with a HayeSep packed column, 2 m in length and 2 millimetres in diameter. The column employed an 80–100 mm mesh and a N_2 carrier gas and used a flame ionisation detector (FID).

Catalysts were examined by X-ray diffraction (XRD), using a Bruker D8 diffractometer with a Cu Kα X-ray source operating at 40 kV and 40 mA, with a scan range of 10–80°2θ, a step size of 0.05°, and a scan time of 30 min. Surface morphology and elemental distribution were evaluated using Hitachi SU8230 scanning electron microscopy (SEM) operated at 2.0 kV and combined with an Oxford Instrument, Aztec energy-dispersive X-ray spectroscopy (EDX) for fresh and used Bi-Metallic catalysts. SEM-EDX was employed to generate high-resolution images and to confirm the elemental composition of the sample. The patterns of carbon deposition and coke oxidation on the used catalysts were analysed by temperature-programmed oxidation (TPO). These characterisations facilitated the assessment of how the active metal phase and metal–support interaction affected structural stability, dispersion, and coke resistance before and after catalytic reforming. To evaluate the statistical reliability of the reactor system, variance metrics including standard deviation (STD) and relative standard deviation (RSD) were calculated. As a baseline, repeated tests were carried out using 1.0 g of polypropylene and the 10 wt% Ni/Al_2O_3 catalyst under uniform reaction parameters. These repeat experiments confirmed excellent experimental consistency. The mass balance across the system averaged 98.83 wt%, demonstrating minimal fluctuation with a low STD of 1.59 and an RSD of just 1.61%. Similarly, the yields for the main product phases remained highly stable; the average gas fraction (42.38 wt%) and liquid fraction (55.98 wt%) recorded narrow RSD values of 2.53% and 4.21%,

respectively. This data verifies that the reactor and condensation assemblies accurately and reproducibly captured the material flow. While the solid char deposits displayed a broader relative variance, such fluctuations were related to the negligible trace quantities (averaging just 0.46 wt%) of the produced char. Furthermore, error bars representing the STD have been included in all experimental H_2 yield figures to explicitly establish the statistical reliability and consistency of the results across all tested catalyst formulations.

3 | Results and Discussion

3.1 | Establishing Optimum Metal Loading

Initial work established the optimum metal loading on the catalysts by using Ni-Al_2O_3 with different metal loadings from 0 to 40 wt%. The freshly prepared catalysts, reduced catalysts (reduced with hydrogen), and the used catalysts after the pyrolysis-catalytic steam reforming of waste polypropylene were characterised using X-ray diffraction (XRD) to determine the crystallite size of the metal particles using the Scherrer equation. The results are shown in Table 2.

Crystallite sizes remain small across the calcined, reduced, and used catalyst samples. For 5 wt%, the Ni particles are 7.3, 7.2, and 5.2 nm, and for 10 wt% Ni, they are 7.5, 8.1, and 8.7 nm, respectively. This indicates well-dispersed Ni and agrees with earlier work that reported NiO near 63° with crystallites of 6.1 and 6.6 nm in calcined samples for 5 and 10 wt% Ni, respectively [18].

TABLE 2 | Catalyst crystallite sizes of freshly prepared, reduced, and used Ni/Al_2O_3 catalysts with different nickel loadings in relation to the catalytic pyrolysis-steam reforming of waste polypropylene.

	Crystallite size, nm		
Metal loading, wt%	**Fresh**	**Reduced**	**Used**
Al_2O_3	4.8	—	5.3
5 wt% Ni	7.3	7.2	5.2
10 wt% Ni	7.5	8.1	8.7
20 wt% Ni	7.2	31.3	35.9
30 wt% Ni	27.5	58.5	46.6
40 wt% Ni	41.7	40.8	69.2

At higher nickel loadings, the crystallite size of the metal particles dramatically increases, particularly for the reduced catalysts. For example, the metal particle size for the reduced catalyst increases from 8.1 nm at 10 wt% nickel loading to 31.3 nm at 20 wt%, 58.5 nm at 30 wt%, and to 40.8 nm at 40 wt%. The increased particle size suggesting that there is agglomeration of the nickel on the surface of the catalyst at high loading, reducing the availability of the nickel catalyst active sites for the pyrolysis volatiles reforming reactions. In addition, the used catalyst showed large crystallite particle size ranging from 35.9 to 69.2 nm as the metal loading was increased from 20 to 40 wt%.

The Ni-Al_2O_3 catalysts with different amounts of nickel were used for the catalytic steam reforming of polypropylene in the two-stage pyrolysis-catalytic steam reforming reactor system. The overall total gas yield for the experiments showed that the gas yield for alumina alone was 41.76 wt%, and the addition of nickel showed a modest increase in total gas yield as nickel was added, reaching a maximum of 45.41 at 40 wt% nickel loading. The results in relation to gas composition and gas yield are shown in Table 3. The results show that even in the presence of alumina, without any active Ni metal present, the H_2 yield was 57.75 mmol $g^{-1}_{plastic}$, but H_2 yield markedly increases in the presence of Ni, reaching a maximum of 105.17 at 10 wt% Ni loading. This notable performance increase confirms that the impregnation of Ni provides the free active sites required for rapid sequential C—H and C—C bond cleavage. The high dispersion of Ni at 10 wt% (as seen in XRD) maximises the surface area for primary hydrocarbon adsorption, successfully shifting the thermodynamic equilibrium towards hydrogen-rich syngas by driving the formyl (CHO) intermediate gasification pathway [19]. The H_2:CO molar ratio was a maximum of 2.43 at 10 wt% Ni loading. The Al_2O_3 support material acts mainly as a surface for hydrocarbon volatiles adsorption and thermal polymerisation rather than as an active reforming catalyst. But the results demonstrate that the addition of metals remains essential for activating steam reforming, improving syngas quality. Increasing the nickel loading above 10 wt% did not have an improvement in H_2 yield or H_2:CO molar gas ratio. Increasing Ni loadings produced higher CO yields and a consequent decrease in H_2:CO molar gas ratio. Also noteworthy is the yield of unreformed methane and heavier CnHm molecular weight hydrocarbons, which were higher at low Ni loadings (O wt% and 5 wt%) and at higher Ni loadings (20, 30, and 40 wt%). Artetxe et al. [20], using a pyrolysis-catalytic steam reforming process for hydrogen production from waste plastic also reported that an intermediate Ni loading maximised

TABLE 3 | Gas composition and gas yield (mmol $g^{-1}_{plastic}$), and H_2:CO and H_2:CO_2 gas ratios from the pyrolysis-catalytic steam reforming of waste polypropylene in relation to nickel catalyst loading.

	Gas yield, mmol $g^{-1}_{plastic}$					Gas ratios	
	H_2	**CO**	**CO_2**	**CH_4**	**C_nH_m**	**H_2:CO**	**H_2:CO_2**
Al_2O_3	57.75	27.47	8.85	16.94	8.85	2.10	6.53
5 wt% Ni	94.56	39.8	4.88	11.23	1.43	2.38	19.38
10 wt% Ni	105.17	43.25	5.8	8.45	0.97	2.43	18.13
20 wt% Ni	99.27	46.79	6.03	7.75	3.43	2.12	16.46
30 wt% Ni	102.03	47.8	7.02	7.48	3.00	2.13	14.53
40 wt% Ni	99.49	47.95	6.91	8.54	4.10	2.07	14.41

hydrocarbon steam reforming and that higher Ni loadings produced higher catalyst coke formation through CO disproportionation on larger Ni particles. The drop in performance at higher loadings (20–40 wt%) is directly tied to the thermal sintering and crystallite expansion observed in the XRD data (up to 69.2 nm). This severe agglomeration reduces the availability of active sites, hindering the primary cracking steps, which revert the system to incomplete secondary gasification and increase the yield of unreacted methane.

Therefore, the optimum metal loading for the study of bimetallic catalysts was deemed to be 10 wt% (5 wt% of each bi-metal), based on the high H yield, low CO yield, higher H_2:CO molar ratio, and lowest yield of unreformed hydrocarbons. In addition, the XRD data shows that at the higher Ni-loadings, the particle size of the active metals tends to sinter/agglomerate, producing large metal particle sizes.

Figure 2 shows the experimental H_2 yield (g $100\,g^{-1}_{plastic}$) produced from the pyrolysis-catalytic steam reforming of polypropylene in relation to the theoretical maximum H_2 yield obtained from the waste plastic (equivalent to 44.1 g H_2 $100\,g^{-1}_{polypropylene}$) for the catalysts with different Ni loadings. The maximum theoretical hydrogen yield assumes that all of the carbon and hydrogen in polypropylene is converted to H_2 and CO_2 via the steam reforming process, which was calculated directly from the ultimate analysis of the polypropylene feedstock. The alumina support material acted as a catalyst to some extent producing 11.6 g H_2 per $100\,g^{-1}_{plastic}$ (polypropylene) representing 26.4% of the maximum theoretical hydrogen yield with a high experimental standard deviation (STD) of 8.27. The influence of nickel addition to produce the Ni/Al_2O_3 catalysts, resulted in an increase in the yield of H_2, ranging from 19.1 g H_2 per $100\,g^{-1}_{plastic}$ to 21.2 g H_2 per $100\,g^{-1}_{plastic}$, representing a range of 43.2% to 48.1% of the maximum theoretical H_2 yield. Crucially, the introduction of active Ni sites significantly reduced experimental variance; for example, the optimal 10 wt% Ni catalyst achieved its 48.1% peak efficiency with a low STD of 3.34, demonstrating the shift from uncontrolled, fluctuating thermal scission to stable, directed catalytic reforming.

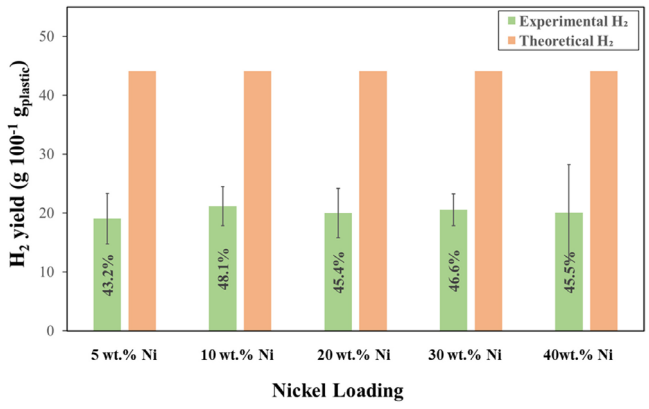

FIGURE 2 | The experimental H_2 yield (g $100\,g^{-1}_{plastic}$) produced from the pyrolysis-catalytic steam reforming of polypropylene in relation to the theoretical maximum H_2 yield obtained from the waste plastic. Also shown is the percentage experimental yield.

3.2 | Bimetallic Catalyst Characterisation

The bimetallic catalysts used for the pyrolysis-catalytic steam reforming of waste polypropylene were characterised using X-ray diffraction (XRD) to determine their crystalline structures, alongside scanning electron microscopy coupled with energy dispersive X-ray spectroscopy (SEM-EDX) to evaluate surface morphology and elemental dispersion. Figure 3 shows the XRD spectra of the 10 wt% Ni/Al_2O_3 catalyst, and Figure 4 shows the XRD spectra of the Ni-based bimetallic catalysts across their freshly calcined, reduced, and spent states. Table 4 details the corresponding crystallite sizes calculated using the Scherrer equation. By correlating the XRD crystal phase evolution with localised SEM-EDX elemental mapping, the physical stability and phase segregation of the active metals during the high-temperature reforming process can be elucidated.

Figure 3 shows that for the 10 wt% Ni loading (representing 5−5 wt% Ni) the γ Al_2O_3 peaks remain dominant at 37.0°, 45.9°, 60.8°, and 66.8°. In the calcined state, NiO appears at 37.2°, 43.3°, 62.9°, and 75.4°; however, after reduction, these reflections disappear, and weak metallic Ni peaks emerge at 44.5°, 51.8°, and 76.4°.

3.2.1 | Ni-Fe/Al_2O_3 Catalyst

Figure 4 shows the XRD spectra of the Ni-Fe/Al_2O_3 catalyst (Figure 4a) and shows clear structural changes between the calcined, reduced, and spent states. In the unreduced catalyst, NiO reflections appear near 37° and 43° in 2θ, while Fe_2O_3 gives peaks at 33°, 36°, and 54°, all overlapping the broad γ-Al_2O_3 reflections at 37°, 46°, and 67°. After reduction, the oxide peaks disappear, and new reflections at 44.3° and 51.7° develop, consistent with the formation of an Ni-Fe alloy. Similar behaviour is reported for other Ni-Fe/Al_2O_3 systems, where Fe incorporation shifts the Ni peak to lower 2θ and generates Ni-rich or Fe-rich alloy phases, depending on the composition [21]. After the pyrolysis-catalytic steam reforming process, the FeNi peaks persist but broaden, indicating some redistribution or encapsulation of alloy

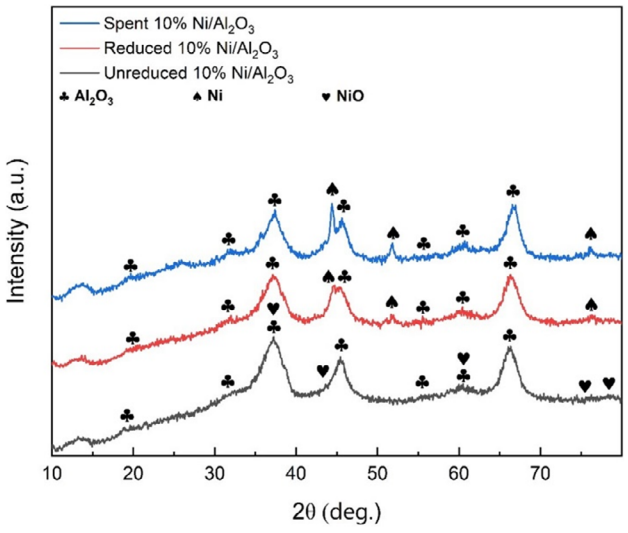

FIGURE 3 | X-ray diffraction spectra of freshly prepared, reduced and used 10 wt% Ni/Al_2O_3 (5 wt% Ni-5 wt% Ni) catalyst.

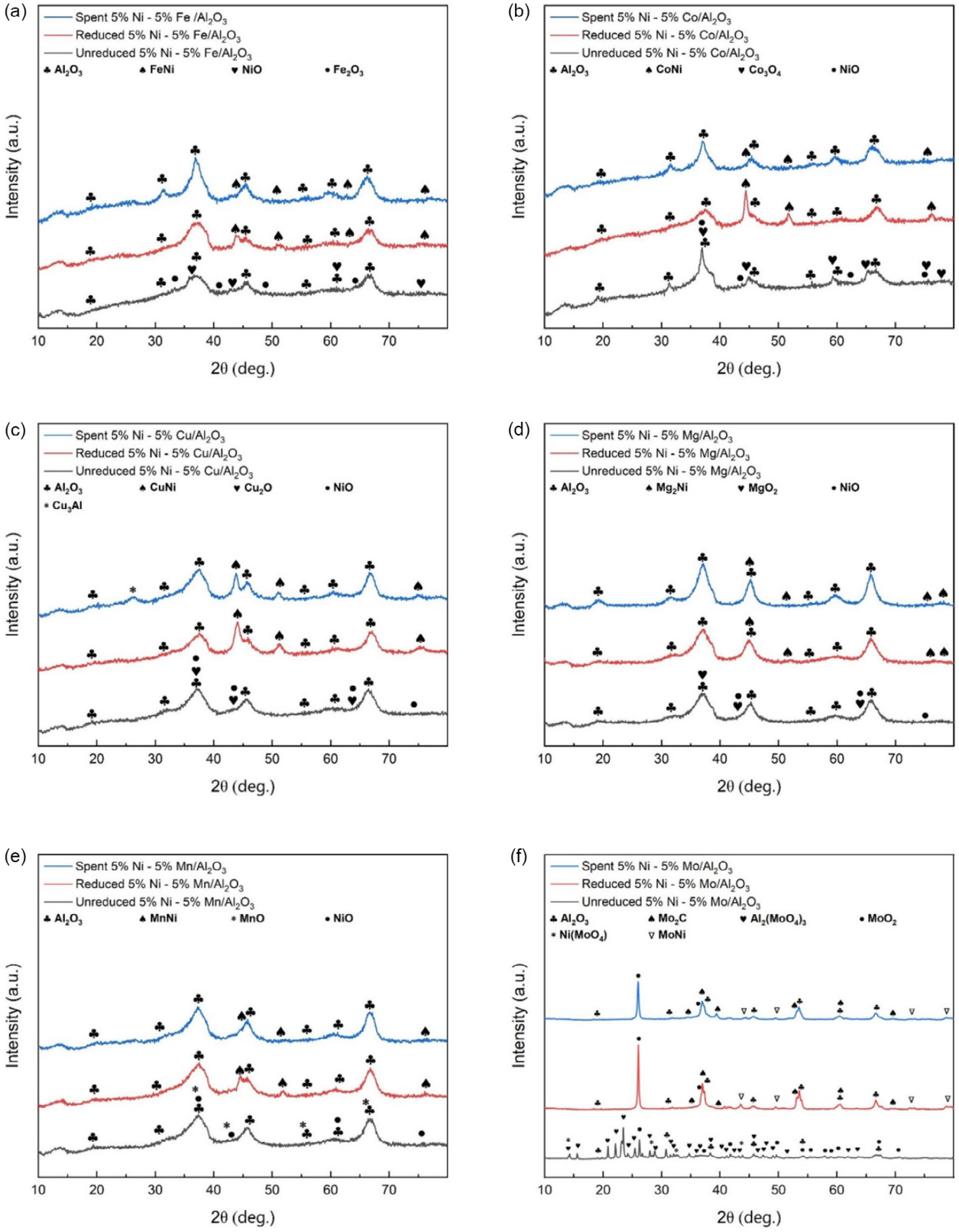

FIGURE 4 | X-ray diffraction (XRD) spectra of freshly prepared, reduced, and used Ni-based bimetallic-Al_2O_3 catalysts used in the pyrolysis-catalytic steam reforming of polypropylene. (a) Ni-Fe/Al_2O_3, (b) Ni-Co/Al_2O_3, (c) Ni-Cu/Al_2O_3, (d) Ni-Mg/Al_2O_3, (e) Ni-Mn/Al_2O_3, and (f) Ni-Mo/Al_2O_3.

particles during the reaction. Comparable trends have been observed in chemical looping reforming, where NiFe peaks weaken after prolonged operation, and on $MgAl_2O_4$-supported NiFe catalysts, where FeNi reflections and 2θ shifts after reduction confirm the incorporation of both metals [21, 22]. Crystallite size (Table 4) analysis reveals a distinctive contraction from 9.6 nm in the calcined state to 8.1 nm after reduction and 6.7 nm in the spent state, indicating that Fe incorporation

TABLE 4 | Bi-metallic catalysts crystallite sizes of freshly prepared, reduced, and used catalysts used for catalytic pyrolysis-steam reforming of waste polypropylene.

Catalyst	Crystallite size, nm		
	Fresh	Reduced	Used
Ni-Ni/Al_2O_3	7.5	8.1	8.7
Ni-Fe/Al_2O_3	9.6	8.1	6.7
Ni-Co/Al_2O_3	15.8	14.8	13.5
Ni-Cu/Al_2O_3	6.2	8.6	11.4
Ni-Mg/Al_2O_3	6.9	10.6	7.2
Ni-Mn/Al_2O_3	4.1	4.8	4.3
Ni-Mo/Al_2O_3	112.3	65.3	46.6
Mn-Mo/Al_2O_3	78.5	33.0	31.3
Fe-Co/Al_2O_3	9.4	5.3	7.3
Co-Cu/Al_2O_3	11.8	7.4	8.8

induces structural stabilisation rather than thermal sintering. SEM-EDX mapping supports this, revealing a local Ni/Fe ratio ranging from 0.77 to 0.78 in the fresh catalyst, indicating surface enrichment by Fe driven by its oxophilic nature and lower surface free energy [23]. After reaction, the Ni/Fe ratio drops further to 0.72–0.75, confirming that Fe continues to segregate to the outermost surface to facilitate the redox cycle without causing severe bulk agglomeration.

3.2.2 | *Ni-Co/Al_2O_3 Catalyst*

For the Ni-Co/Al_2O_3 catalyst, the XRD spectra (Figure 4b) show that for the unreduced sample, NiO reflections occur near 2θ values of 37°, 44°, and 65°, while Co_3O_4 gives peaks at 31°, 36°, and 59°, alongside γ-Al_2O_3 features at 37°, 46°, and 67°. These patterns suggest spinel-type phases such as $CoAl_2O_4$, $NiCo_2O_4$, and Co_3O_4 [24]. After reduction, NiO and Co_3O_4 peaks vanish, and new peaks near 2θ of 44.5° and 51.8° confirm CoNi alloy formation, in line with literature on reduced Ni-Co catalysts [25]. The alloy peaks remain in the used catalyst sample but broaden slightly, indicating that the alloy stays largely intact during reforming while some surface redistribution occurs. Crystallite sizes (Table 4) decrease from 15.8 nm in the calcined catalyst to 14.8 nm after reduction and 13.5 nm after reaction. The persistence of alloy peaks also contrasts with monometallic references, where stronger Co-related reflections at 36.6°, 42.88°, and 52.3° are assigned to Co_3O_4 or $CoAl_2O_4$ [26]. The combination of stable alloy peaks and consistent crystallite sizes for the Ni-Co/Al_2O_3 catalyst therefore highlights a synergistic stabilising effect that resists sintering more effectively than either Ni or Co alone. SEM-EDX elemental maps confirm that Ni and Co are effectively co-dispersed, with the local Ni/Co ratio shifting minimally from 1.08 to 1.12 in the fresh state to 1.05–1.07 in the spent state. This nanoscale homogeneity and structural preservation are linked to the specific carbon mitigation properties of Co; carbon has a lower diffusion coefficient in Co compared to Ni, which forces carbon to extrude outwards via a vapour-liquid-solid (VLS) base growth mechanism rather than dissolving and encapsulating the particle [27–31].

3.2.3 | *Ni-Cu/Al_2O_3 Catalyst*

The XRD spectra of the Ni-Cu/Al_2O_3 catalyst (Figure 4c) show for the unreduced sample, NiO peaks appear with Cu_2O peaks, broad γ-Al_2O_3 features and weak Cu_3Al signals, consistent with earlier reports of NiO, CuO, Cu_2O, γ-Al_2O_3, θ-Al_2O_3, and Cu_3Al phases on Ni-Cu/Al_2O_3 catalysts [32]. After reduction, most NiO and Cu_2O peaks weaken, and new alloy-type peaks develop, confirming oxide reduction, and the formation of an Ni-Cu alloy. For the used catalyst the alloy peaks remain, with slight sharpening and intensity changes that indicate the alloy structure persists during the reforming reaction. The crystallite size (Table 4) increases from 6.2 nm in the calcined sample to 8.6 nm after reduction and 11.4 nm after reforming, indicating moderate sintering. SEM-EDX analysis reveals that while the fresh catalyst displays a uniform initial distribution (Ni/Cu ratio of 1.07–1.12), the spent catalyst exhibits progressive crystallite growth and a shifted Ni/Cu ratio (1.13–1.16). Because Cu possesses a low Tammann temperature (405°C) [33], Ostwald ripening initiates under reforming temperatures (800°C) [34], causing the alloy to struggle to maintain structural integrity, which leads to partial phase dissociation and progressive sintering.

3.2.4 | *Ni-Mg/Al_2O_3 Catalyst*

The Ni-Mg/Al_2O_3 catalyst shows XRD spectra (Figure 4d) that for the calcined sample, NiO 2θ values appear at 37.2°, 43.3°, and 62.9°, accompanied by broad γ-Al_2O_3 peaks at 37°, 46°, and 67°. Extra signals at 43° and 62° correspond to MgO_2. This matches reports on Ni Mg Al systems that describe spinel phases such as $NiAl_2O_4$ and $MgAl_2O_4$ after calcination, together with MgO periclase and Mg(NiAl)O solid solutions identified through peak shifts near 43° [35, 36]. After reduction, NiO peaks fade, and Mg_2Ni alloy peaks near 44° and 51.6° Mg_2Ni alloy peaks appear, confirming Ni Mg phase formation. The crystallite size increases from 6.9 nm in the unreduced state to 10.6 nm after reduction as NiO is converted into metallic and alloyed structures. After reforming, the spent catalyst retains Mg_2Ni features, demonstrating that the alloy remains stable. The crystallite size then falls slightly to 7.2 nm, which is opposite to the growth commonly observed in Ni/Al_2O_3 systems, indicating that Mg incorporation limits Ni agglomeration and stabilises the structure. Similar stabilisation has been reported for hydrotalcite-derived NiMg/Al_2O_3, where Ni^{2+} incorporation into MgO lattices slows crystallite growth and strengthens metal-support bonding [35, 36]. Overall, the persistence of Mg_2Ni peaks at all stages and the reduced crystallite size in the spent catalyst underline the role of Mg in enhancing Ni dispersion and resisting deactivation. SEM-EDX mapping supports this structural resilience, showing a homogeneous metal distribution with a high Ni/Mg ratio that evolves minimally from 1.62 to 1.78 in the fresh state to 1.76–1.79 in the spent state. This consistent distribution indicates good initial anchoring and strong metal–support interactions that prevent active phase agglomeration.

3.2.5 | *Ni-Mn/Al_2O_3 Catalyst*

The XRD patterns of the Ni-Mn/Al_2O_3 catalyst (Figure 4e) show for the calcined sample, NiO 2θ values at 37.2°, 43.3°, and 62.9° lie on γ-Al_2O_3 2θ peaks near 37°, 46°, and 67°, while additional signals at 34° and 40° indicate MnO. After reduction, the NiO

peaks weaken, and alloy-type peaks at 44.2° and 51° appear, consistent with the formation of NiMn and a strong interaction between the two metals. Crystallite sizes change only slightly at ~4 nm. The XRD spectra of the used Ni-Mn/Al_2O_3 catalyst retain MnNi alloy and γ-Al_2O_3 peaks, confirming alloy stability under catalytic steam reforming conditions. The absence of $NiAl_2O_4$ phases suggests the role of Mn in dispersing Ni and preventing the formation of strong Ni-Al spinels [37]. SEM-EDX analysis reveals uniform angular particles with the local Ni/Mn ratio shifting marginally from 1.05 to 1.07 in the fresh state to 1.11–1.12 after reaction. This high dispersion preserves the active metallic surface and confirms the role of Mn as a structural stabiliser that mitigates severe Ni sintering.

3.2.6 | Ni-Mo/Al_2O_3 Catalyst

The XRD analysis of the Ni-Mo/Al_2O_3 catalyst in Figure 4f shows that the calcined sample has strong $NiMoO_4$ 2θ peaks that appear together with γ-Al_2O_3 peaks at 37°, 46°, and 67° and MoO_2 2θ values at 27° and 55°, matching reports of coexisting $NiMoO_4$ and MoO_2 before activation [38]. After reduction, the $NiMoO_4$ peaks weaken, and new peaks emerge, assigned to MoNi alloy (44.6°, 50.0°) [39]. Crucially, an active Mo_2C phase also forms, evidenced by reflections at 39.3°, 52.1°, and 61.5° [40]. A slight shift of the γ-Al_2O_3 peak towards lower angles indicates some Ni incorporation into the support, with Mo moderating this interaction and limiting $NiAl_2O_4$ spinel formation, in line with earlier observations [38]. Crystallite size analysis shows formation of large crystallite sizes of 112.3 nm in the calcined state, reducing to 65.3 nm after reduction, and then to 46.6 nm in the used catalyst. However, SEM-EDX mapping demonstrates a clear morphological trade-off. Mo extensively covers the support and masks the Ni active sites, with the local Ni/Mo ratio dropping from 0.42 to 0.47 in the fresh state to 0.32–0.34 in the spent catalyst. This physical masking restricts the primary C—C bond cleavage efficiency of Ni, which subsequently impacts overall gasification.

3.3 | Characterisation of Other Bimetallic Catalysts

X-ray diffraction (XRD) characterisation of the non-nickel-containing bimetallic catalysts (Mn-Mo/Al_2O_3, Fe-Co/Al_2O_3, and Co-Cu/Al_2O_3) was carried out for the freshly prepared and reduced catalysts in addition to the used catalysts after the pyrolysis-catalytic steam reforming process of polypropylene. The resultant XRD spectra are shown in Figure 5.

3.3.1 | Mn-Mo/Al_2O_3 Catalyst

The XRD spectra of the Mn-Mo/Al_2O_3 catalyst shown in Figure 5a exhibit, for the calcined sample, $Mn_2Mo_3O_8$ 2θ peaks at 23°, 27°, 36°, and 41°, together with $Mn(MoO_4)$, MoO_2, and alumina-supported molybdate phases, such as $Al_2(MoO_4)_3$, at 29°–31° and 47°, confirming the presence of mixed Mn-Mo oxide species before reduction. After reduction, the molybdate peaks weaken, while active Mo_2C reflections emerge at 39.3°, 52.1°, and 61.5°, and Mn oxides persist, consistent with the higher reduction resistance of Mn. The crystallite size (Table 4) decreases from 78.5 nm in the calcined state to 33.0 nm after reduction, as large oxide particles break down into smaller

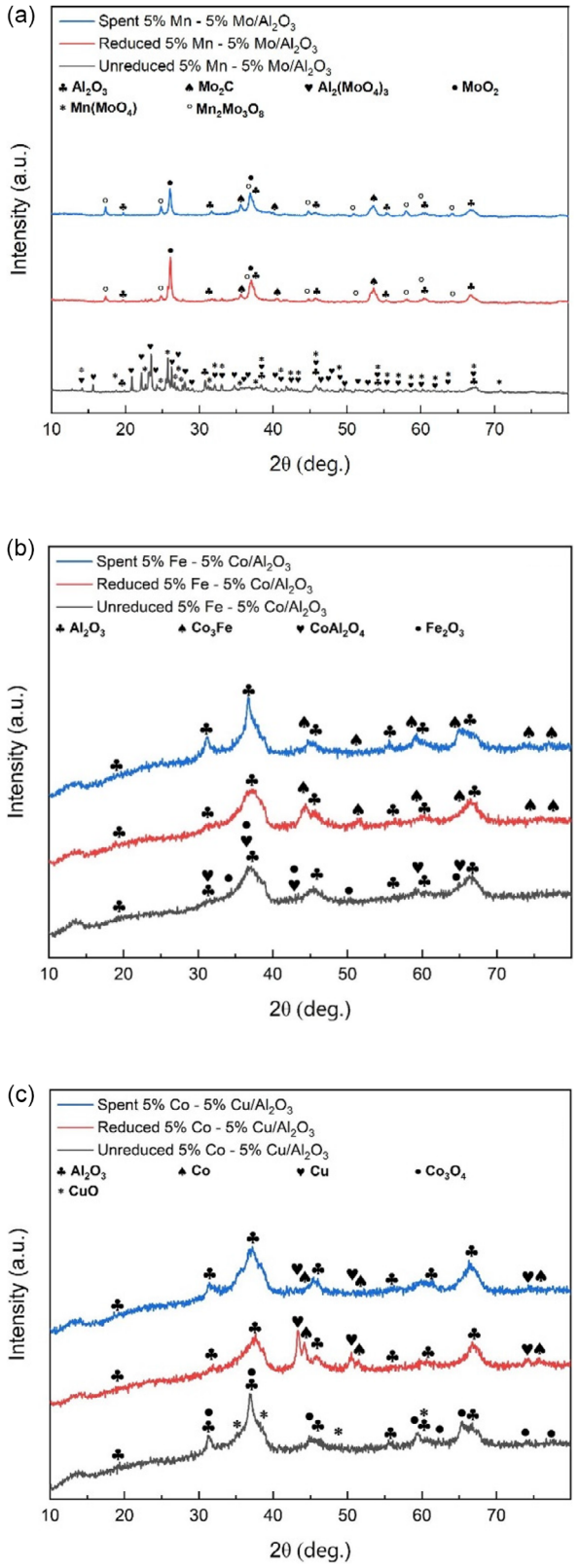

FIGURE 5 | X-ray diffraction (XRD) spectra of freshly prepared, reduced and used bimetallic-Al_2O_3 catalysts used in the pyrolysis-catalytic steam reforming of polypropylene. (a) Mn-Mo/Al_2O_3, (b) Fe-Co/Al_2O_3, and (c) Co-Cu/Al_2O_3.

nanoparticles. After reforming, Mo remains stable while Mn 2θ peaks fade and the size contracts slightly to 31.3 nm, suggesting limited sintering and maintained dispersion under reaction

conditions. Literature indicates that Mo suppresses the presence of bulky MnOx and enhances MnOx-support interactions, thereby improving dispersion and anchoring on γ-Al_2O_3 [41]. This explains why particle sizes, although reduced upon activation, remain stable after reforming and why Mo steadily moderates the structural effects of Mn. SEM-EDX mapping reveals a consistently low Mn/Mo ratio (0.28–0.29 in the fresh state and 0.27–0.28 in the spent state). This indicates that Mo heavily masks the surface, severely limiting access to any active sites and preventing efficient hydrocarbon breakdown.

3.3.2 | *Fe–Co/Al_2O_3 Catalyst*

The XRD spectra of the freshly prepared Fe-Co/Al_2O_3 catalyst, as shown in Figure 5b, indicate Fe_2O_3 2θ peaks at 33°, 36°, and 54° appear with γ-Al_2O_3 peaks. Similar Fe_2O_3 features are reported in the literature, often alongside Co_3O_4 and $CoAl_2O_4$ spinels at 2θ peaks at 31.2° and 36.7° [42]. Weak reflections around 44° to 45° already indicate the formation of a Co-Fe alloy, in line with alloy peaks near 45.15° that signal early Co incorporation and initial metal–metal interaction during activation [43]. For the used catalyst, alloy peaks persist with only limited broadening, demonstrating structural stability. This agrees with methane decomposition studies, where Fe-Co alloys remained visible after reaction, while spinel signals grew due to partial reoxidation or phase growth [44]. Such durability is often attributed to spinel layers, such as $CoAl_2O_4$ and Fe_3O_4, on alumina, which restricts redistribution and helps suppress sintering. SEM-EDX mapping, however, reveals that this surface synergy is partially disrupted during reforming. In the fresh state, the Fe/Co ratio ranges from 1.69 to 1.84, reflecting surface enrichment by Fe due to its lower surface free energy and high oxophilicity. After reaction, this ratio drops to 1.14–1.15. This indicates that Fe partially migrates into the oxygen-rich alumina bulk under reforming conditions, which ultimately disrupts the combined cracking synergy of the two metals.

3.3.3 | *Co-Cu/Al_2O_3 Catalyst*

The XRD spectra of the Co-Cu/Al_2O_3 catalyst are shown in Figure 5c) and show contributions from cobalt and copper phases on γ-Al_2O_3. In the calcined state, Co_3O_4 reflections at 31°, 36°, 59°, and 65° appear together with CuO peaks at 35.5° and 38.7°, in agreement with studies where CuO and Co_3O_4 were detected after calcination of CuCoAl mixed metal oxides [45]. After reduction, the CuO peaks vanish, and metallic Cu reflections appear at 43.3° and 50.4°, accompanied by metallic Co reflections at 44.2° and 51.5°, confirming the conversion from oxides to separate metallic Cu and Co species. This matches earlier work on Cu-Co ratios of 5:1 in CO hydrogenation, where distinct Cu and Co peaks were assigned to separate metals rather than solid solutions [45]. The average crystallite size decreases from 11.8 nm in the calcined sample to 7.4 nm after reduction. After reforming, the used catalyst particle size rises slightly to 8.8 nm, indicating limited sintering and good dispersion. Similar studies report Cu-only catalysts with particles near 13.2 nm, while balanced Cu-Co compositions reach smaller domains around 9.2 nm, suggesting that cobalt contributes to size control and structural stability [45]. In the used Co-Cu/Al_2O_3 catalyst, metallic Co and Cu peaks remain alongside γ-Al_2O_3 peaks, confirming separate metallic phases with no alloy formation. SEM-EDX mapping reveals a critical surface dynamic driving this separation. The local Co/Cu ratio is consistently low (0.80–0.82 in the fresh state; 0.83–0.86 in the spent state). This indicates that Cu migrates to the outer surface to form a coating layer over the Co particles. Because Cu lacks the empty d-orbitals required to cleave strong C—C bonds, this surface segregation physically masks the active Co cracking sites.

3.4 | Influence of Bimetallic Catalysts on the Pyrolysis-Catalytic Steam Reforming of Polypropylene

The product yield from the two-stage pyrolysis-catalytic steam reforming of polypropylene in relation to the different bimetallic catalysts used in the second-stage catalytic reforming reactor was determined, and the results are shown in Table 5. The mass of each metal was 5 wt% for each of the catalyst active metals, resulting in a total mass of 10 wt% of the bimetals. All of the process conditions were kept the same throughout the experiments, with a mass of polypropylene at 1.0 g, catalyst mass of 1.0 g (plastic:catalyst ratio of 1:1), the polypropylene pyrolysis temperature was a maximum of 500°C, the catalyst temperature was maintained at 800°C, and the input steam-to-plastic flow rate was 4 g/h.

The results presented in Table 5 were calculated in terms of the mass balance based on the input plastic, the liquid collected in the condensers, and the solids representing the char collected after the experiments. The results show that the total gas yield in relation to all of the bimetallic catalysts produced a gas yield between 32.84 and 42.39 wt%. The liquid was almost entirely condensed water from the steam input, with only a trace (<0.2 wt%) of unreformed hydrocarbon oil. The solids consisted of residual char produced from the pyrolysis of the plastic condensed high molecular weight tar/solid deposited on the walls of the catalytic reactor. The 5 wt% Ni-5 wt% Ni (10 wt% Ni) catalyst showed the highest yield of gas, as did the Ni-Fe and Ni-Mn bimetallic catalysts. Those nickel-based bimetallic catalysts with reduced gas yields included Ni-Co, NiCu, and to some extent Ni-Mo. The three bimetallic catalysts that did not contain nickel, Mn-Mo,

TABLE 5 | Product yield mass balance from the pyrolysis-catalytic steam reforming of waste polypropylene in relation to different bimetallic catalysts.

	Product yield, wt%		
	Gas	**Liquid**	**Solids**
Ni–Ni/Al_2O_3	42.38	55.98	0.46
Ni-Fe/Al_2O_3	42.39	51.59	0.48
Ni-Co/Al_2O_3	36.94	56.85	0.36
Ni-Cu/Al_2O_3	36.72	59.51	0.76
Ni-Mg/Al_2O_3	39.25	56.96	0.78
Ni-Mn/Al_2O_3	42.39	57.48	0.22
Ni-Mo/Al_2O_3	41.20	54.99	0.23
Mn-Mo/Al_2O_3	32.84	63.02	0.23
Fe-Co/Al_2O_3	33.98	60.94	0.44
Co-Cu/Al_2O_3	35.62	59.60	0.22

Fe-Co, and Co-Cu, all produced significantly lower yields of gas, of 32.84, 33.98, and 35.62 wt%, respectively. These variations in gas and liquid fractions are fundamentally dictated by the specific surface mechanisms of the combined metals. For instance, the reduced gas yield and elevated liquid fraction (54.99 wt%) for Ni-Mo are a direct consequence of Mo structurally masking the Ni sites (as observed in SEM-EDX), which inhibits the primary C—C bond cleavage required to crack heavy plastic volatiles. Similarly, the high liquid fractions for Mn-Mo, Fe-Co, and Co-Cu are driven by the complete absence of an aggressive cracking metal like Ni, combined with physical masking (e.g., the Cu shell over Co). Without accessible active sites for deep dissociation, unreacted heavy hydrocarbons simply condense into liquid waxes rather than reforming into syngas.

An additional presentation of the product yield data is shown in Table 6, where the gas yield is presented in terms of the mass of polypropylene and the reacted water, that is, the total input amount of water minus the mass of condensed water collected in the condensers. This represents a more accurate representation of the catalytic steam reforming process, taking into account the input mass of plastic and water and the output gas yield. The amount of reacted water is also shown in Table 6. The data show clearly the large amount of gas that is produced from the actual catalytic steam reforming of the polypropylene, ranging from 87.05 wt% (Fe-Co/Al_2O_3) to 99.58 wt% (Ni-Mn/Al_2O_3). Table 6 also shows the total gas yield in relation to the Mass of input polypropylene only, where the yield is well over 100 wt%, approaching 200 wt%. This data shows that a substantial amount of the product gas arises from the input steam, which could be regarded as a low-cost input reactant in the process. The extent of this steam consumption highlights the mechanistic pathways operating on the catalyst surface. Systems like Ni-Fe, Ni-Co, and Ni-Mo show high reacted water values (~0.99–1.01 g g^{-1} plastic), which validates the efficiency of their respective redox and MvK (Mars-van-Krevelen) cycles [46–50]. These metals constantly consume steam to refill surface oxygen vacancies. Conversely, the low steam consumption for Mn-Mo (0.64 g g^{-1}) perfectly aligns with its poor primary cracking rate; without cracked intermediates to gasify, steam activation is heavily suppressed.

The detailed analysis of the product gases obtained from all the experiments from the pyrolysis-catalytic steam reforming of polypropylene in relation to the bimetallic catalysts is shown in Table 7. The highest hydrogen yield was obtained with the Ni-Al_2O_3 catalyst (5 wt% Ni-5 wt% Ni; 10 wt% Ni) at 105.17 mmol $g^{-1}_{plastic}$ and with a syngas H_2:CO yield of 2.43. High hydrogen yields were also produced with the Ni-Co/Al_2O_3 and Ni-Cu/Al_2O_3 at 100.50 Ni $g^{-1}_{plastic}$ and 99.13 Ni $g^{-1}_{plastic}$, respectively. The yield of hydrogen from the other bimetallic catalysts that did not contain any nickel was significantly lower. The Co-Cu/Al_2O_3 catalyst gave a H_2 yield of 70.72 mmol $g^{-1}_{plastic}$, the Fe-Co/Al_2O_3 catalyst had a H_2 yield of 74.70 mmol $g^{-1}_{plastic}$, and the Mn-Mo catalyst produced the lowest H_2 yield at only 60.16 mmol $g^{-1}_{plastic}$.

Table 7 also shows the H_2:CO and H_2:CO_2 molar gas ratios. The H_2:CO ratio is an important parameter for the downstream end-use applications of the syngas and is influenced by the composition of the feedstock, the hydrogen production process, the reforming gas (e.g., steam or CO_2), the type of catalyst, and process conditions such as temperature and pressure. Further post-production stages, such as the water-gas shift reaction ($CO + H_2O \leftrightarrow H_2 + CO_2$) or gas purification, such as membrane separation, can further alter the H_2:CO molar ratio. The ratio produced from the pyrolysis-catalytic steam reforming of the waste polypropylene in relation to the different bimetallic catalysts ranged from 1.96 for the Ni-Mo catalyst to 3.41 for the Ni-Cu catalyst. These distinct shifts in syngas composition are controlled by the unique thermodynamic and oxygen-shuttling pathways introduced by the secondary metals. In the Ni-Fe, Ni-Co, and Ni-Mn systems, the secondary metal actively dissociates steam to form mobile lattice oxygen. Consistent with the MvK and redox cycles described in the literature [46–50], this oxygen is continuously shuttled to adjacent Ni sites to rapidly gasify atomic carbon into CO. For Ni-Mn, this is combined with the thermodynamic promotion of the Reverse Water Gas Shift (RWGS) reaction at 800°C, which actively consumes CO_2 and H_2 to form CO and steam [51], explaining its heavily suppressed CO_2 yield (5.13 mmol g^{-1}). Alternatively, for the Ni-Mg system, the balanced shift towards CO and H_2 (at the expense of CO_2) is driven

TABLE 6 | Gas yield, in terms of the mass of polypropylene and reacted water, in terms of the mass of polypropylene only and the amount of reacted water from the bimetallic catalysed pyrolysis-catalytic steam reforming of polypropylene.

Bimetallic catalyst	Gas yield (Polypropylene + reacted water), wt%	Gas yield (Polypropylene only), wt%	Reacted water, g $g^{-1}_{plastic}$
Ni-Ni/Al_2O_3	96.72	184.51	0.92
Ni-Fe/Al_2O_3	87.94	176.47	1.01
Ni-Co/Al_2O_3	85.55	170.54	0.99
Ni-Cu/Al_2O_3	90.63	161.33	0.78
Ni-Mg/Al_2O_3	91.21	170.87	0.87
Ni-Mn/Al_2O_3	99.58	191.19	0.92
Ni-Mo/Al_2O_3	91.51	183.32	1.00
Mn-Mo/Al_2O_3	88.83	145.96	0.64
Fe-Co/Al_2O_3	87.05	152.92	0.76
Co-Cu/Al_2O_3	88.09	159.44	0.81

TABLE 7 | Gas yield (mmol $g^{-1}_{plastic}$), and H_2:CO and H_2:CO_2 gas ratios from the pyrolysis-catalytic steam reforming of waste polypropylene in relation to different bimetallic catalysts.

	Gas yields, mmol $g^{-1}_{plastic}$				Gas ratios		
	H_2	CO	CO_2	CH_4	C_nH_m	H_2:CO	H_2:CO_2
Ni-Ni/Al_2O_3	105.17	43.25	5.80	8.45	0.97	2.43	18.13
Ni-Fe/Al_2O_3	94.68	41.85	5.06	9.1	0.61	2.26	18.71
Ni-Co/Al_2O_3	100.50	33.71	7.07	11.91	1.79	2.98	14.21
Ni-Cu/Al_2O_3	99.13	29.06	8.56	12.12	0.92	3.41	11.58
Ni-Mg/Al_2O_3	92.19	36.03	5.86	11.26	2.32	2.56	15.73
Ni-Mn/Al_2O_3	87.55	40.99	5.13	16.67	3.11	2.14	17.07
Ni-Mo/Al_2O_3	82.26	41.91	5.37	12.28	3.35	1.96	15.32
Mn-Mo/Al_2O_3	60.16	30.10	3.19	10.32	5.76	2.00	18.87
Fe-Co/Al_2O_3	74.70	23.38	8.17	14.37	4.30	3.19	9.14
Co-Cu/Al_2O_3	70.72	29.63	5.75	12.13	5.45	2.39	12.29

by the surface basicity of Mg. As observed in previous oxygenated reforming studies [52, 53], Mg Lewis basic sites chemisorb acidic CO_2 to form surface carbonates, which subsequently react with adjacent atomic carbon via the reverse Boudouard reaction ($CO_2 + C \rightleftharpoons 2CO$), consuming CO_2 to generate additional CO. In contrast, the Ni-Cu system lacks a strong oxygen-shuttling mechanism but provides highly active sites for the Water-Gas Shift (WGS) reaction [54]. Adsorbed CO undergoes nucleophilic activation by surface hydroxyls, converting CO into CO_2 and releasing extra H_2, which explains its uniquely high H_2:CO ratio of 3.41. Finally, despite poor total conversion, the Ni-free systems (Fe-Co and Co-Cu) produce balanced syngas through secondary modulation. Fe-Co utilises a combined redox gasification pathway (MvK via Co and WGS via Fe), while Co-Cu relies on the outer shell of Cu to drive WGS, while the underlying Co slowly partially oxidises fragments.

Fischer–Tropsch gas to liquid fuels (gasoline or diesel) ideally require a H_2:CO molar ratio of 2:1, but the range can be 1.7:1 to 2.2:1 [55–57]. The production of chemicals from syngas also depends on an optimum H_2:CO ratio; for example, methanol requires a ratio between 1.5:1 and 2:1, aldehydes and ethers require an optimum H_2:CO ratio of 1:1 [55, 56, 58, 59]. Hydrogen-rich syngas with a H_2:CO molar ratio of >3.0 would be attractive for use in combustion efficiency and would reduce carbon dioxide emissions.

Figure 6 shows the experimental H_2 yield (g 100 $g^{-1}_{plastic}$) produced from the pyrolysis-catalytic steam reforming of polypropylene in relation to the theoretical maximum H_2 yield obtained from the waste plastic (equivalent to 44.11 g H_2 100 $g^{-1}_{polypropylene}$) for the bimetallic catalysts. The theoretical hydrogen yield is based on the ultimate analysis of the polypropylene feedstock.

The bimetallic catalysts show that the maximum theoretical hydrogen yield was 21.2 g H_2 per 100 $g^{-1}_{plastic}$, obtained from the Ni-Ni/Al_2O_3 catalyst, representing 48.1% of the maximum theoretical H_2 yield (STD = 3.34). Other bimetallic catalysts also showed high yields of hydrogen (in terms of g H_2 per 100 $g^{-1}_{plastic,}$), for example, the Ni-Fe/Al_2O_3 catalyst (19.1 g H_2 per 100 $g^{-1}_{plastic}$, STD = 6.64), Ni-Co/Al_2O_3 catalyst (20.3 g H_2 per

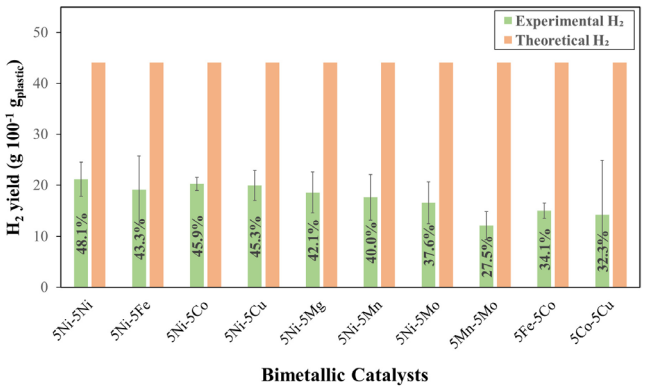

FIGURE 6 | Experimental H_2 yield (g 100 $g^{-1}_{plastic}$) produced from the pyrolysis-catalytic steam reforming of polypropylene in relation to the theoretical maximum H_2 yield for the bimetallic catalysts. Also shown is the percentage experimental yield in relation to the theoretical yield for each catalyst.

100 $g^{-1}_{plastic}$, STD = 1.29) and Ni-Cu/Al_2O_3 catalyst (20.0 g H_2 per 100 $g^{-1}_{plastic}$, STD = 2.93), representing between 44.3%, 45.9% and 45.3% of the theoretical H_2 production, respectively. The Ni-Mg/Al_2O_3 catalyst achieved 42.1% efficiency (STD = 3.98), while the Ni-Mn/Al_2O_3 and Ni-Mo/ Al_2O_3 systems achieved 40.0% (STD = 4.42) and 37.6% (STD = 4.09), respectively. Some of the other bimetallic catalysts produced significantly lower yield of hydrogen, for example, Ni-Mo/Al_2O_3 and the non-nickel containing catalysts Mn-Mo/Al_2O_3, Fe-Co/Al_2O_3, and Co-Cu/Al_2O_3 catalysts recorded theoretical H_2 yields of 27.5% (STD = 2.79), 34.1% (STD = 1.48), and 32.3% (STD = 10.61), respectively. These differing efficiencies and variance profiles represent strategic structural trade-offs. The high efficiency and stability of Ni-Co (45.9%, STD 1.29) and Ni-Fe (43.3%) demonstrates that sacrificing a small amount of primary cracking activity (relative to Mono 10Ni) enables continuous carbon gasification and prevents deactivation. Conversely, the low efficiencies and high variance of certain Ni-free systems (e.g., Co-Cu at 32.3%, STD 10.61) represent the kinetic limitation created by surface segregation (Fe migrating into the bulk, Cu forming an inert shell), which forces the system to rely on uncontrolled thermal

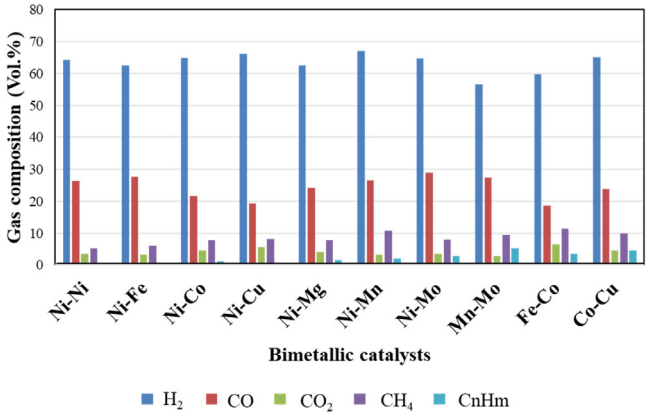

FIGURE 7 | Gas composition (vol%) from the pyrolysis-catalytic steam reforming of waste polypropylene in relation to different bimetallic catalysts.

cracking to initiate volatile decomposition. In contrast, the highly stable Fe-Co pairing maintained low variance (STD 1.48) despite its low conversion (34.1%), indicating a controlled, albeit slower, reforming environment. An additional note, as suggested by Czernik and French [60], is that the H_2 yield could be further increased by adding a water gas shift reactor downstream of the catalytic steam reforming stage of the pyrolysis-catalytic steam reforming process for waste plastics. The substantial amount of carbon monoxide produced in the stream reforming of the plastics pyrolysis volatiles, of up to 43.25 mmol CO $g^{-1}_{plastic}$.

$$CO + H_2O \rightleftharpoons CO_2 + H_2 \quad (2)$$

In the commercial production of hydrogen from the catalytic steam reforming of natural gas, methane, the presence of a downstream water gas shift reactor system (high temperature, followed by low temperature shift reactors), is typical. Czernik and French [60] suggest that the addition of such a shift reactor could boost the H_2 yield from the processing of waste polypropylene by 10%–12%

The volumetric composition of the product gases is also an important parameter, particularly in relation to the use of the syngas as a gaseous fuel, and the results for the pyrolysis-catalytic steam reforming of polypropylene with the different bimetallic catalysts are shown in Figure 7. The volumetric gas composition showed that all the catalysts produced high H_2 and CO yields, particularly for the nickel-containing catalysts where H_2 was between 62.5 and 70 vol%, and CO was ~25 vol%. The catalysts that did not contain any nickel, Mn-Mo, Fe-Co, and Co-Cu produced volumetric H_2 concentration of 54.9, 59.8, and 57.1 vol%, respectively. The three catalysts also showed relatively higher yields of unreformed CH_4 and CnHm hydrocarbons, as was also the case for the Ni-Mn bimetallic catalyst. The composition of the combustible syngas produced a mean higher heating value of 116.7 MJ kg^{-1}, ranging from 112.0 MJ kg^{-1} (Fe-Co catalyst) to 121.2 MJ kg^{-1} (Ni-Ni) catalyst.

3.5 | Catalyst Coke Deposition

An important factor in the use of catalysts for the pyrolysis-catalytic steam reforming process is the potential for catalyst deactivation due to the deposition of byproduct carbonaceous coke on the catalysts which can lead to catalyst deactivation due to the reduced availability of the active catalyst metals. Table 8 shows the coke deposition on the bimetallic catalysts after use in the two-stage pyrolysis-catalytic steam reforming reactor system, determined via temperature programmed oxidation using thermogravimetric analysis in an oxidising atmosphere (air). The oxidation of the catalyst during the raising of the temperature in the thermogravimetric analysis procedure can indicate the presence of amorphous carbons, which oxidise at lower temperatures, or filamentous carbons, which oxidise at high temperatures [10]. This TPO analysis establishes a direct quantitative relationship between coke deposition, coke morphology, and the catalyst's specific synergy mechanisms.

TABLE 8 | Carbonaceous coke deposition on the bimetallic catalysts after use in the pyrolysis-catalytic steam reforming of polypropylene.

Catalyst	Catalyst coke deposition, wt%
Ni-Ni/Al_2O_3	9.34
Ni-Fe/Al_2O_3	7.71
Ni-Co/Al_2O_3	5.38
Ni-Cu/Al_2O_3	15.76
Ni-Mg/Al_2O_3	6.60
Ni-Mn/Al_2O_3	5.62
Ni-Mo/Al_2O_3	0.36
Mn-Mo/Al_2O_3	0.41
Fe-Co/Al_2O_3	2.71
Co-Cu/Al_2O_3	4.49

Catalyst coke deposition on the Ni-Ni catalyst was 9.34 wt%, and the TPO thermogram indicated a higher temperature oxidation of the carbon (~600°C), indicating more filamentous carbon rather than amorphous [10]. In contrast, the Ni-Fe catalyst recorded a true net coke loss of 7.71 wt% with a primary oxidation peak at 583°C, indicating less ordered, defective carbon. This reduction demonstrates that the continuous supply of lattice oxygen from the Fe redox cycle [61] successfully gasifies accumulating carbon before it forms structured graphitic shells. Similarly, the Ni-Co catalyst exhibited a significantly reduced coke load of 5.38 wt% (oxidation peak at 603°C), directly validating the ability of Co to supply surface oxygen via the MvK cycle to gasify atomic carbon while simultaneously promoting VLS carbon extrusion [27, 28]. Conversely, the Ni-Cu catalyst recorded a high 15.76 wt% coke loss with a peak at 523°C (dense amorphous carbon). Because Cu segregates and lacks a strong redox cycle to supply lattice oxygen, isolated Ni sites crack hydrocarbons faster than they can be gasified, leading to rapid site masking and deactivation. In contrast, the coke deposition on the Ni-Mg catalyst was 6.60 wt%, with oxidation peaking at an elevated 625°C. While this indicates highly structured graphitic/filamentous carbon, it proves that Mg basicity forces carbon to grow as non-deactivating crystalline filaments rather than encapsulating amorphous coke, preserving the exposed Ni sites for continuous steam dissociation [62, 63]. The Ni-Mn catalyst exhibited a coke deposit of just 5.62 wt% with a lower oxidation peak (523°C). This confirms that

the multivalent redox capacity of Mn rapidly shuttles lattice oxygen to atomic carbon, immediately gasifying it into CO before it can polymerise into resilient filamentous shells [64]. The most active carbon suppression was observed in the Mo-based systems. Ni-Mo and Mn-Mo recorded negligible true net coke losses of 0.36 wt% and 0.41 wt%, respectively, completely masked by weight gains (up to 4.07 wt%) from bulk Mo reoxidation (Mo^0 to MoO_3). The presence of the Mo_2C phase detected in XRD enables a highly active Type II MvK mechanism [65]. Mo restricts the dissolution of carbon into the metal particles entirely; however, because the primary cracking sites are masked by Mo, the minimal carbon that does form simply condenses as soft amorphous coke on the surface. The Ni-free bimetallic combinations exhibited distinct coke behaviours tied to their structural limitations. The Fe-Co catalyst produced a low coke deposit of 2.71 wt%. Its TPO oxidation profile was broad and continuous up to 700°C (primary peak at 572°C), indicating progressive combustion of mixed, defective carbon species. The continuous supply of lattice oxygen from Fe and surface oxygen from Co rapidly gasifies atomic carbon before it can polymerise into dense encapsulating graphite. In contrast, the Co-Cu catalyst produced 4.49 wt% coke with a low-temperature primary peak at 450°C, indicating soft amorphous carbon. Because the inert Cu shell physically masks the Co active sites (as shown by SEM-EDX) and prevents deep catalytic cracking, unreacted heavy hydrocarbons simply condense onto the catalyst surface as an amorphous carbon layer.

4 | Conclusions

Bimetallic catalysts on Al_2O_3 support have been investigated for the pyrolysis-catalytic steam reforming of waste polypropylene in relation to the production of hydrogen, H_2:CO syngas ratio, and catalyst coke formation. The findings demonstrate that while a well-distributed nickel phase serves as the fundamental requirement for deep C—C bond cleavage, its performance and longevity are majorly governed by the synergistic mechanisms introduced by secondary metals.

Among the tested formulations, the monometallic Ni/Al_2O_3 (10 wt% Ni) was the most effective for enhanced conversion, giving the highest hydrogen yield of 105.17 mmol g^{-1} plastic. However, at higher nickel loadings (20–40 wt%), the system was inhibited by marked crystallite growth and severe active site agglomeration, causing a decline in catalytic efficiency and an increase in unreformed hydrocarbons. The introduction of secondary metals successfully mitigated these deactivation pathways through distinct surface mechanisms. Redox-driven gasification proved highly effective, as seen with the Ni-Co/Al_2O_3 catalyst, which produced a high hydrogen yield (100.50 mmol g^{-1} plastic), an H_2:CO ratio of 2.98, and low coke deposition (5.38 wt%). This enhanced performance is driven by a stable alloy that forces carbon into a VLS extrusion mechanism, while Co executes an MvK redox cycle to continuously supply surface oxygen for carbon gasification. Similarly, the Ni-Fe/Al_2O_3 catalyst (94.68 mmol g^{-1} plastic) maintained low unreformed hydrocarbon levels and average coking (7.71 wt%) through a dynamic Fe redox cycle, where iron segregates to the surface to supply lattice oxygen. Furthermore, the Ni-Mn/Al_2O_3 catalyst (87.55 mmol g^{-1} plastic) utilised an MvK oxygen shuttle combined with the thermodynamic promotion of the reverse water gas shift reaction to actively suppress CO_2 formation and limit carbon to easily oxidised defective coke.

Enhancing catalyst basicity offered another successful carbon management pathway. The Ni-Mg/Al_2O_3 catalyst yielded a H_2 production of 92.19 mmol g^{-1} plastic with a balanced H_2:CO_2 ratio (2.56) and reduced coke deposition (6.60 wt%). This resilience was attributed to stable Mg_2Ni alloy formation and increased support basicity; the Mg Lewis basic sites chemisorb CO_2 to drive the reverse Boudouard reaction, actively consuming carbon and forcing any remaining deposits into non-deactivating crystalline filaments.

Other bimetallic pairings demonstrated more extreme structural trade-offs. The Ni-Mo/Al_2O_3 catalyst (82.26 mmol g^{-1} plastic) demonstrated an effective tolerance to carbon deposition (0.36 wt%) through highly oxophilic, Mo-centred Type II MvK redox behaviour. However, this came at the cost of overall gasification, as Mo physically masked the Ni active sites, restricting primary C—C cleavage and increasing liquid fractions. Conversely, the Ni-Cu/Al_2O_3 catalyst achieved the highest H_2:CO ratio of 3.41 by providing highly active surface sites that promoted the water gas shift reaction. Because Cu suffered from Ostwald ripening and lacked an oxygen-shuttling mechanism, the isolated Ni sites accumulated massive amounts of dense amorphous coke (15.76 wt%), leading to rapid deactivation.

Bimetallic catalysts without the presence of Ni (Fe-Co, Co-Cu, Mn-Mo) fundamentally lacked the necessary primary C—C cleavage capacity, yielding high liquid wax fractions and significantly lower hydrogen volumes. For example, the Fe-Co/Al_2O_3 catalyst produced 74.70 mmol g^{-1} plastic. Despite low total conversion, it maintained a high H_2:CO molar ratio of 3.19 and efficient coke resistance (2.71 wt%) through secondary syngas modulation, utilising a combined MvK (via Co) and water gas shift (via Fe) pathway. Similarly, the Co-Cu/Al_2O_3 system relied on an inert Cu outer shell to drive water gas shift activity while masking the underlying Co core. These results guide future catalyst design by identifying that maximising hydrogen yield and syngas quality from plastic waste requires balancing the cracking ability of Ni with carefully selected synergistic bimetal pairings that provide targeted redox, basicity, or water gas shift pathways.

Author Contributions

Fayez Alshehri: investigation, methodology, writing – original draft preparation. **Paul T. Williams**: supervision, writing – reviewing and editing.

Acknowledgments

F. A., is a PhD Researcher at the University of Leeds, and his scholarship is sponsored and supported by the Ministry of Education of the Saudi Arabian Government and King Abdulaziz City for Science and Technology. The authors would also like to thank the Leeds Electron Microscopy and Spectroscopy (LEMAS) centre. Within the Bragg

Centre for Materials Research at the University of Leeds for help with SEM-EDXS and XRD analysis.

Funding

The authors have nothing to report.

Conflicts of Interest

The authors declare no conflicts of interest.

Data Availability Statement

The data that support the findings of this study are available from the corresponding author upon reasonable request.

References

1. OECD, "Global Plastics Outlook, OECD," Accessed November 6, 2025, https://www.oecd.org/en/publications/global-plastics-outlook_de747aef-en.html.

2. F. Suleman, I. Dincer, and M. Agelin-Chaab, "Environmental Impact Assessment and Comparison of Some Hydrogen Production Options," *International Journal of Hydrogen Energy* 40, no. 21 (2015): 6976–6987.

3. Hydrogen Newsletter, "GH2 Facts: CO_2 Emissions per Kg of Hydrogen Depending on the Method of Production," Accessed 2025, https://www.hydrogennewsletter.com/gh2-facts/.

4. I. Dincer and C. Acar, "Review and Evaluation of Hydrogen Production Methods for Better Sustainability," *International Journal of Hydrogen Energy* 40, no. 34 (2015): 11094–11111.

5. Y. R. Kannah, S. Kavitha, O. Preethi, et al., "Techno-Economic Assessment of Various Hydrogen Production Methods – A Review," *Bioresource Technology* 319 (2021): 124175.

6. P. T. Williams, "Hydrogen and Carbon Nanotubes from Pyrolysis-Catalysis of Waste Plastics: A Review," *Waste & Biomass Valorization* 12 (2021): 1–28.

7. M. Shah H.H.Amin, A. Iqbal, I. Nadeem, M. Kalin, A. M. Soomar, and A. M. Galal, "A Review on Gasification and Pyrolysis of Waste Plastics," *Frontiers in Chemistry* 10 (2023): 960894.

8. L. Santamaria, G. Lopez, E. Fernandez, et al., "Progress on Catalyst Development for the Steam Reforming of Biomass and Waste Plastics Pyrolysis Volatiles: A Review," *Energy and Fuels* 35, no. 21 (2021): 17051–17084.

9. P. T. Williams and E. A. Williams, "Interaction of Plastics in Mixed Plastics Pyrolysis," *Energy and Fuels* 13 (1999): 188–196.

10. C. Wu and P. T. Williams, "Investigation of Coke Formation on Ni-Mg-Al Catalyst for Hydrogen Production from the Catalytic Steam Pyrolysis-Gasification of Polypropylene," *Applied Catalysis B: Environmental* 96, no. 1-2 (2010): 198–207.

11. I. Barbarias, G. Lopez, J. Alvarez, et al., "Valorisation of Different Waste Plastics by Pyrolysis and in-Line Catalytic Steam Reforming for Hydrogen Production," *Energy Conversion and Management* 156 (2018): 575–584.

12. M. He, B. Xiao, Z. Hu, S. Liu, X. Guo, and S. Luo, "Syngas Production from Catalytic Gasification of Waste Polyethylene: Influence of Temperature on Gas Yield and Composition," *International Journal of Hydrogen Energy* 34, no. 2 (2009): 1342–1348.

13. W. C. Williams, "Effects of Gasification Temperature and Catalyst Ratio on Hydrogen Production from Catalytic Steam Pyrolysis-Gasification of Polypropylene," *Energy and Fuels* 22, no. 11 (2008): 4125–4132.

14. C. Wu and P. T. Williams, "Hydrogen Production from the Pyrolysis-Gasification of Polypropylene: Influence of Steam Flow Rate, Carrier Gas Flow Rate and Gasification Temperature," *Energy & Fuels* 23 (2009): 5055–5061.

15. A. Gupta, R. Kumar, J. P. Sharma, M. H. Ahmadi, J. Ni, and L. Prokop, "The Role of Catalyst in Hydrogen Production: A Critical Review," *Journal of Thermal Analysis and Calorimtery* 149 (2024): 14517–14534.

16. M. D. Argyle and C. H. Bartholomew, "Heterogeneous Catalyst Deactivation and Regeneration: A Review," *Catalysts* 5 (2015): 145–269.

17. J. Sehested, "Four Challenges for Nickel Steam Reforming Catalysts," *Catalysis Today* 111 (2006): 103–110.

18. A. D. Di Michele A. Angello, A. Tripodi, E. Bahadori, et al., "Steam Reforming of Ethanol over Ni/MgAl2O4 Catalysts," *International Journal of Hydrogen Energy* 44, no. 2 (2019): 952–964.

19. K. Hou and R. Hughes, "The Kinetics of Methane Steam Reforming over a Ni/α-Al2O3 Catalyst," *Chemical Engineering Journal* 82 (March 2001): 311–328.

20. M. Artetxe, J. Alvarez, M. A. Nahil, M. Olazar, and P. T. Williams, "Steam Reforming of Different Biomass Tar Model Compounds over Ni/Al2O3 Catalysts," *Energy Conversion and Management* 136 (2017): 119–126.

21. L. Wang, D. Li, M. Koike, et al., "Catalytic Performance and Characterization of Ni-Fe Catalysts for the Steam Reforming of Tar from Biomass Pyrolysis to Synthesis Gas," *Applied Catalysis A: General* 392, no. 1 (2011): 248–255.

22. T. P. N. Lara, D. D. Petrolini, K. de Oliveira Rocha, J. B. O. dos Santos, and J. M. C. Bueno, "In Situ Study of Structural Modifications in Ni-Fe/MgAl2O4 Catalysts Employed for Ethanol Steam Reforming," *Fuel* 373 (2024): 132336.

23. T. R. Ribeiro, J. B. F. Neto, J. G. R. Poço, C. Takano, L. Kolbeinsen, and E. Ringdalen, "Steam Reforming of Methane on Sponge Iron: Influence of Gas Composition on Reaction Rate," *ISIJ International* 61, no. 1 (2021): 182–189.

24. L. He, H. Berntsen, E. O. Fernandez, J. C. Malmsley, E. A. Blekkan, and D. Chen, "Co–Ni Catalysts Derived from Hydrotalcite-Like Materials for Hydrogen Production by Ethanol Steam Reforming," *Topics in Catalysis* 52 (2009): 206–217.

25. A. Lysne, K. O. Madsen, J. Antony, K. R. Rout, and E. A. Blekkan, "Effects of Ni-Co Ratio on Deactivation and Coke Formation in Steam Reforming of Hydrocarbon Impurities from Biomass Gasification with Ni-Co/Mg(Al)O Catalysts," *Chemical Engineering Transactions* 92 (2022): 37–42.

26. S. Andonova, C. N. de Ávila, A. Arishtirova, J. M. C. Bueno, and S. Damyanova, "Structure and Redox Properties of Co Promoted Ni/Al2O3 Catalysts for Oxidative Steam Reforming of Ethanol," *Applied Catalysis B: Environmental* 105, no. 3-4 (2011): 346–360.

27. W. Zhang, J. Zhao, L. Wang, G. Liu, D. Shen, and H. Zhang, "Crystal-Facet Effect of γ-Al2O3 on Fe–Al2O3 Catalytic Performance for the Co-Production of Hydrogen and CNTs from Catalytic Reforming of Toluene," *International Journal of Hydrogen Energy* 58 (March 2024): 1466–1477.

28. S. Chen, J. Zaffran, and B. Yang, "Dry Reforming of Methane over the Cobalt Catalyst: Theoretical Insights into the Reaction Kinetics and Mechanism for Catalyst Deactivation," *Applied Catalysis B: Environmental* 270 (August 2020): 118859.

29. S. Mizuno, J. Horiuchi, K. P. Sharma, T. Saida, and T. Maruyama, "In Situ XAFS Study on the Chemical States of Transition-Metal Nanoparticle Catalysts during Single-Walled Carbon Nanotube Growth under Conventional CVD Conditions,"Journal," *Nanoparticle Research* 27 (June 2025): 155.

30. A. Lysne, K. O. Madsen, J. Antony, K. R. Rout, and E. A. Blekkan, "Effects of Ni-Co Ratio on Deactivation and Coke Formation in Steam Reforming of Hydrocarbon Impurities from Biomass Gasification with Ni-Co/Mg(Al)O Catalysts," *Chemical Engineering Transactions* 92 (June 2022): 37–42.

31. Z. Ferencz, E. Varga, R. Puskás, et al., "Reforming of Ethanol on Co/Al2O3 Catalysts Reduced at Different Temperatures," *Journal of Catalysis* 358 (February 2018): 118–130.

32. M. Khzouz, J. Wood, K. Kendall, and W. Bujalski, "Characterization of Ni–Cu-Based Catalysts for Multi-Fuel Steam Reformer," *International Journal Low-Carbon Technology* 7, no. 1 (2012): 55–59.

33. X. Zheng, Q. Su, W. Mi, and P. Zhang, "Effect of Steam Reforming on Methanefueled Chemical Looping Combustion with Cu-Based Oxygen Carrier," *International Journal of Hydrogen Energy* 39 (June 2014): 9158–9168.

34. Q.-L. Tang and Z.-P. Liu, "Identification of the Active Cu Phase in the Water Gas Shift Reaction over Cu/ZrO2 from First Principles," *The Journal of Physical Chemistry C* 114 (May 2010): 8423–8430.

35. D. Li, L. Wang, M. Koike, Y. Nakagawa, and K. Tomishige, "Steam Reforming of Tar from Pyrolysis of Biomass over Ni/Mg/Al Catalysts Prepared from Hydrotalcite-Like Precursors," *Applied Catalysis B: Environmental* 102, no. 3 (2011): 528–538.

36. S. Kumagai, R. Yabuki, T. Kameda, Y. Saito, and T. Yoshioka, "Simultaneous Recovery of H2-Rich Syngas and Removal of HCN during Pyrolytic Recycling of Polyurethane by Ni/Mg/Al Catalysts," *Chemical Engineering Journal* 361 (2019): 408–415.

37. W. L. Vrijburg, G. Garbarino, W. Chen, et al., "Ni-Mn Catalysts on Silica-Modified Alumina for CO2 Methanation," *Journal of Catalysis* 382 (2020): 358–371.

38. T. Borowiecki, W. Gac, and A. Denis, "Effects of Small MoO3 Additions on the Properties of Nickel Catalysts for the Steam Reforming of Hydrocarbons," *Applied Catalysis A: General* 270, no. 1 (2004): 27–36.

39. V. Claude, J. G. Mahy, R. G. Tilkin, and S. D. Lambert, "Enhancement of the Catalytic Performances and Lifetime of Ni/γ-Al2O3 Catalysts for the Steam Toluene Reforming via the Combination of Dopants: Inspection of Cu, Co, Fe, Mn, and Mo Species Addition," *Materials Today Chemistry* 15, no. #100229, 2020.

40. T. Huang, W. Huang, J. Huang, and P. Ji, "Methane Reforming Reaction with Carbon Dioxide over SBA-15 Supported Ni–Mo Bimetallic Catalysts," *Fuel Processing Technology* 92 (October 2011): 1868–1875.

41. G. Yang, H. Zhao, X. Luo, et al., "Promotion Effect and Mechanism of the Addition of Mo on the Enhanced Low Temperature SCR of NOx by NH3 over MnOx/γ-Al2O3 Catalysts," *Applied Catalysis B: Environmental* 245 (2019): 743–752.

42. H. Jia, L. Yang, H. Zhu, et al., "Co–Fe/Al2O3 Catalyst for Low-Temperature Steam Reforming of Phenol for Hydrogen Production," *International Journal of Hydrogen Energy* 86 (2024): 751–761.

43. T. Das and G. Deo, "Promotion of Alumina Supported Cobalt Catalysts by Iron," *The Journal of Physical Chemistry C* 116, no. 39 (2012): 20812–20819.

44. T. V. Reshetenko, L. B. Avdeeva, A. A. Khassin, et al., "Coprecipitated Iron-Containing Catalysts (Fe-Al2O3, Fe-Co-Al2O3, Fe-Ni-Al2O3) for Methane Decomposition at Moderate Temperatures: Part II. Evolution of the Catalysts in Reaction," *Applied Catalysis A: General* 270, no. 1-2 (2004): 87–99.

45. W. Gao, Y. Zhao, H. Chen, et al., "Core–shell Cu@(CuCo-Alloy)/Al2O3 Catalysts for the Synthesis of Higher Alcohols from Syngas," *Green Chemistry* 17, no. 3 (2015): 1525–1534.

46. M. Koike, Y. Hisada, L. Wang, et al., "High Catalytic Activity of Co-Fe/α-Al2O3 in the Steam Reforming of Toluene in the Presence of Hydrogen," *Applied Catalysis B: Environmental* 140-141 (August 2013): 652–662.

47. A. Giehr, L. Maier, S. A. Schunk, and O. Deutschmann, "Thermodynamic Considerations on the Oxidation State of Co/γ-Al2O3 and Ni/γ-Al2O3 Catalysts under Dry and Steam Reforming Conditions," *Chem-CatChem* 10, no. 4 (2018): 751–757, https://chemistryeurope.onlinelibrary.wiley.com/doi/pdf/10.1002/cctc.201701376.

48. K. N. Papageridis, G. Siakavelas, N. D. Charisiou, et al., "Comparative Study of Ni, Co, Cu Supported on γ-Alumina Catalysts for Hydrogen Production via the Glycerol Steam Reforming Reaction," *Fuel Processing Technology* 152 (November 2016): 156–175.

49. H. Sohn and U. S. Ozkan, "Cobalt-Based Catalysts for Ethanol Steam Reforming: An Overview," *Energy & Fuels* 30 (July 2016): 5309–5322.

50. B. Chen, S. Rickard, Z. Bao, Z. Wu, M. K. Kidder, and A. Savara, "Evidence of Redox Cycling as a Sub-Mechanism in Hydrogen Production during Ethanol Steam Reforming over La0.7Sr0.3MnO3-x Perovskite Oxide Catalysts," *Applied Surface Science* 617 (April 2023): 156603.

51. M. V. Grabchenko, N. V. Dorofeeva, V. A. Svetlichnyi, et al., "Ni-Based SBA-15 Catalysts Modified with CeMnOx for CO2 Valorization via Dry Reforming of Methane: Effect of Composition on Modulating Activity and H_2/CO Ratio," *Nanomaterials* 13 (January 2023): (2641).

52. A. Jawad, "The Effects of Fe, Mg, and Pt-Doping on the Improvement of Ni Stabilized on Al_2O_3-CeO_3 Catalysts for Methane Dry Reforming," *RSC Advances* 13 (November 2023): 33129–33145.

53. S. Adapa, K. Yuan, B. R. Evans, et al., "Acidities of MgO Surface Sites: Implications for the Formation Mechanism of Mg(OH)2," *Journal of Materials Chemistry A* 13 (August 2025): 27367–27376.

54. O. Akdim, W. Cai, V. Fierro, et al., "Oxidative Steam Reforming of Ethanol over Ni–Cu/SiO2, Rh/Al2O3 and Ir/CeO2:Effect of Metal and Support on Reaction Mechanism," *Topics in Catalysis* 51 (December 2008): 22–38.

55. R. Rauch, J. Hrbek, and H. Hofbauer, "Biomass Gasification for Synthesis Gas Production and Applications of the Syngas," *Wiley Interdisciplinary Reviews: Energy and Environment* 3 (2014): 343–362.

56. X. Song and Z. Guo, "Technologies for Direct Production of Flexible H_2/CO Synthesis Gas," *Energy Conversion & Management* 47, no. 5 (2006): 560–569.

57. T. K. Penny, M. A. Nahil, and P. T. Williams, "Pyrolysis-Catalytic Steam/Dry Reforming of Processed Municipal Solid Waste for Control of Syngas H_2: CO Ratio," *Journal Energy Institute* 102 (2022): 128–142.

58. H. T. Luk, C. Mondelli, D. C. Ferré, J. A. Stewart, and J. Pérez-Ramírez, "Status and Prospects in Higher Alcohols Synthesis from Syngas," *Chemical Society Reviews* 46, no. 5 (2017): 1358–1426.

59. M. H. Huang, H. M. Lee, K. C. Liang, C. C. Tzeng, and W. H. Chen, "An Experimental Study on Single Step Dimethyl-ether (DME) Synthesis from Hydrogen and Carbon Monoxide under Various Catalysts," *International Journal of Hydrogen Energy* 40 (2015): 13583–13593.

60. S. Czernik and R. J. French, "Production of Hydrogen from Plastics by Pyrolysis and Catalytic Steam Reform," *Energy and Fuels* 20 (2006): 754–758.

61. J. Ashok and S. Kawi, "Steam Reforming of Biomass Tar Model Compound at Relatively Low Steam-to-Carbon Condition over CaO-Doped Nickel–iron Alloy Supported over Iron–alumina Catalysts," *Applied Catalysis A: General* 490 (January 2015): 24–35.

62. M. L. Dieuzeide, M. Laborde, N. Amadeo, C. Cannilla, B. Bonura, and F. Frusteri, "Hydrogen Production by Glycerol Steam Reforming: How Mg Doping Affects the Catalytic Behaviour of Ni/Al2O3 Catalysts," *International Journal of Hydrogen Energy* 41, no. 1 (2016): 157–166.

63. L. J. I. Coleman, W. Epling, R. R. Hudgins, and E. Croiset, "Ni/Mg–Al Mixed Oxide Catalyst for the Steam Reforming of Ethanol," *Applied Catalysis A: General* 363, no. 1 (2009): 52–63.

64. S. H. Seok, S. H. Choi, E. D. Park, S. H. Han, and J. S. Lee, "Mn-Promoted Ni/Al2O3 Catalysts for Stable Carbon Dioxide Reforming of Methane," *Journal of Catalysis* 209, no. 1 (2002): 6–15.

65. H. Wang, Y. Diao, Z. Gao, et al., "H_2 Production from Methane Reforming over Molybdenum Carbide Catalysts: From Surface Properties and Reaction Mechanism to Catalyst Development," *ACS Catalysis* 12 (December 2022): 15501–15528.